Research Article | Vol. 27, No. 8 | 15 Apr 2019 | OPTICS EXPRESS 11748
Optics EXPRESS

Silicon photonic add-drop filter based on a grating-assisted co-directionally coupled vertical hybrid structure

MIN-SUK KWON*

School of Electrical and Computer Engineering, Ulsan National Institute of Science and Technology, 50 UNIST-gil, Ulju-gun, Ulsan 44919, South Korea
**mskwon@unist.ac.kr*

Abstract: Add-drop filters (ADFs) are an essential component in optical interconnection using dense wavelength-division multiplexing. Silicon photonic ADFs based on contra-directional coupling have been well developed, but those based on grating-assisted co-directional coupling (GACC) have never been studied. This paper reports an ADF based on GACC in a vertical hybrid structure (VHS). which consists of two width-modulated silicon strip waveguides with a large lateral gap and a wide silicon nitride strip waveguide above them. The VHS makes it possible for the ADF to have a narrow 3-dB bandwidth as well as a short grating length. An efficient analysis method for design is explained, and the ADF is designed. Theoretical investigation of the ADF demonstrates that the ADF has a 3-dB bandwidth of 1.16 nm and a grating length of 1.13 mm, which are similar to those of ADFs based on contra-directional coupling. As an application, the ADF is used for a nonvolatile switchable ADF by adding an optical phase change material strip above the silicon nitride waveguide. The nonvolatile switchable ADF is shown to have an extinction ratio larger than 30 dB. The investigated ADF requires neither waveguides in close proximity nor grating teeth with dimensions close to the resolution of deep UV lithography. In this regard, it has the advantage of ease of fabrication as compared to ADFs based on contra-directional coupling. Therefore, the ADF is expected to play a key role in optical interconnection using dense wavelength-division multiplexing, prevailing over ADFs based on contra-directional coupling.

1. Introduction

Silicon photonics is considered as a key enabling technology for optical interconnection in datacenters and it would even lead to the change of datacenter architecture [1]. As data traffic is tremendously increasing, to keep up with this trend, it is expected that intra-datacenter optical interconnection evolves in the direction of using dense wavelength division multiplexing (DWDM) [2]. Add-drop filters (ADFs) are an essential element for implementation of a DWDM system. Therefore, it is imperative to develop silicon (Si) photonic ADFs with a narrow bandwidth of about 1.6 nm at the telecom wavelength of 1550 nm [2].

A variety of Si photonic ADFs based on contra-directional coupling enabled by a short-period grating have been studied. Asymmetric directional couplers have been used as a basic structure for such ADFs [3–9]. Two Si waveguides with different widths are placed in parallel in a coupling region where the widths are periodically modulated. Qiu *et al*. reported an ADF using a wide Si strip waveguide with a uniform grating and a narrow Si strip waveguide with a phase-modulated grating for apodization [8]. The gap between them is 300 nm wide; the period is 330 nm; the length of the coupling region is 990 μm. The ADF has a 3-dB bandwidth of 0.9 nm. Boroojerdi *et al*. reported a tunable ADF based on dual-stage filtering [9]. It uses gratings in which width-modulation amplitude is apodized. The gap between two Si strip waveguides is 100 nm wide; the period is 312 nm; the length of the coupling region is

#351978 https://doi.org/10.1364/OE.27.011748
Journal © 2019 Received 14 Nov 2018; revised 21 Feb 2019; accepted 29 Mar 2019; published 12 Apr 2019

Optics EXPRESS

303 μm. The 3-dB bandwidth of the ADF is tuned between 0.49 nm and 3.36 nm. When narrow gaps required for asymmetric directional couplers are formed by using 193 or 248 nm deep UV lithography, sufficient care should be taken to prevent the proximity effect [10]. If Si rib waveguides are employed for ADFs, the gap between them can be made larger than 1 μm [3,7]. However, multiple steps of lithography and dry etching should be used to realize those ADFs. Mach-Zehnder interferometers have been also used as a basic structure for ADFs based on contra-directional coupling [11–13]. Two identical Bragg gratings are embedded in the two widely-separated arms of an interferometer. Wang *et al*. reported an interferometer-based ADF which uses uniform gratings with a period of 320 nm and a length of 960 μm [12]. The ADF has a 3-dB bandwidth of 3.4 nm. When ADFs using a Mach-Zehnder interferometer are realized, 3-dB couplers comprising an interferometer may not work ideally [11], or misbalance between two interferometer arms may exist [12]. This causes those ADFs to have poorer characteristics than those expected theoretically. There are another ADFs based on contra-directional coupling in a multimode waveguide [14–16]. Jiang *et al*. reported an ADF using a 1100-nm-wide Si strip waveguide with a phase-modulated grating [14]. The multimode waveguide has contra-directional coupling between the fundamental transverse electric (TE) mode and the counter-propagating first-order TE mode. When the grating has a period of 316 nm and a length of 200 μm, the ADF has a 3-dB bandwidth of 9.5 nm. These types of ADFs have neither the narrow-gap problem nor the misbalance problem, but they require adiabatic mode converters.

ADFs based on contra-directional coupling have their own pros and cons. However, there are two common disadvantages. One is that all the gratings for them have grating teeth with dimensions smaller than ~150 nm. When they are realized on the sidewalls of a Si strip waveguide, they are not rectangular and distorted since the dimensions are close to the resolution of deep UV lithography. This often causes the characteristics of a realized ADF to be inferior to those designed theoretically [4,8,16]. The other disadvantage is that dropped (added) light travels toward the input (through) port of an ADF. Therefore, additional waveguides are required to place the drop (add) port of an ADF close to the through (input) port.

Grating-assisted co-directional coupling (GACC) between two different in-plane Si waveguides can solve the problems of contra-directional coupling. This is because co-propagating modes are coupled to each other via a grating with a long period. However, the two Si waveguides should be still placed in proximity to each other. Most of all, the GACC requires a coupling region with a length of up to a few centimeters for a bandwidth of 1.6 nm since the difference between the group indices of the two Si waveguide modes is usually of the order of 0.1 (see Appendices). This is probably the reason why ADFs based on the GACC have not been studied. This paper reports an ~1-mm-long ADF based on GACC between disparate waveguides, which does not have the narrow-gap problem and require 3-dB couplers or adiabatic mode couplers. For this purpose, the ADF employs a vertical hybrid structure (VHS) in which a layer of silicon nitride (SiN) waveguide devices is vertically stacked on that of Si waveguide devices with a thin silicon dioxide (SiO_2) layer in between. Such a VHS has been developed to merge the advantages of Si waveguide devices (*e.g.*, dense integration and electrical tuning) and those of SiN waveguide devices (*e.g.*, low loss and freedom from two photon absorption) [17–19]. The GACC for the ADF is implemented in a VHS. Previously, GACC in a VHS was used to couple light to a Si waveguide via a silicon oxynitride waveguide and a SiN waveguide [20,21], but it has not been used for Si photonic ADFs yet. In the following, how the ADF is analyzed and designed is explained while an efficient analysis method for design is discussed. Then, the characteristics of the ADF and its fabrication tolerances are presented. Finally, nonvolatile switching of the ADF with an optical phase change material is explained.

Optics EXPRESS

2. ADF structure and analysis methods

The VHS of the investigated ADF consists of two identical conventional Si strip waveguides, laterally well separated, and a wide SiN strip waveguide which is above the center of the two Si strip waveguides. The structure of the ADF is schematically shown in Fig. 1. The ADF is comprised of the input and output sections with only the two Si strip waveguides and the VHS with a grating. For simplicity, it is assumed that all the Si and SiN strips are embedded in SiO_2. The width and height of the Si strips are denoted by W_{Si} and H_{Si}, respectively, which are set at 500 nm and 220 nm. The width and height of the SiN strip are denoted by W_{SiN} and H_{SiN}, respectively. The distance of the lateral gap between the two Si strips is L_{gap}, and the thickness of the vertical gap between the Si and SiN strips is V_{gap}. The grating is formed by increasing the widths of the Si strips by ΔW alternately outwards and inwards in a zig-zag way. The lengths of sub-VHSs 1 and 2 with the Si strips widened outwards and inwards are Λ_1 and Λ_2, respectively, and the period of the grating, Λ is naturally given by $\Lambda_1 + \Lambda_2$. The number of periods is N_p, and the length of the grating section, L_g is given by $N_p \times \Lambda$.

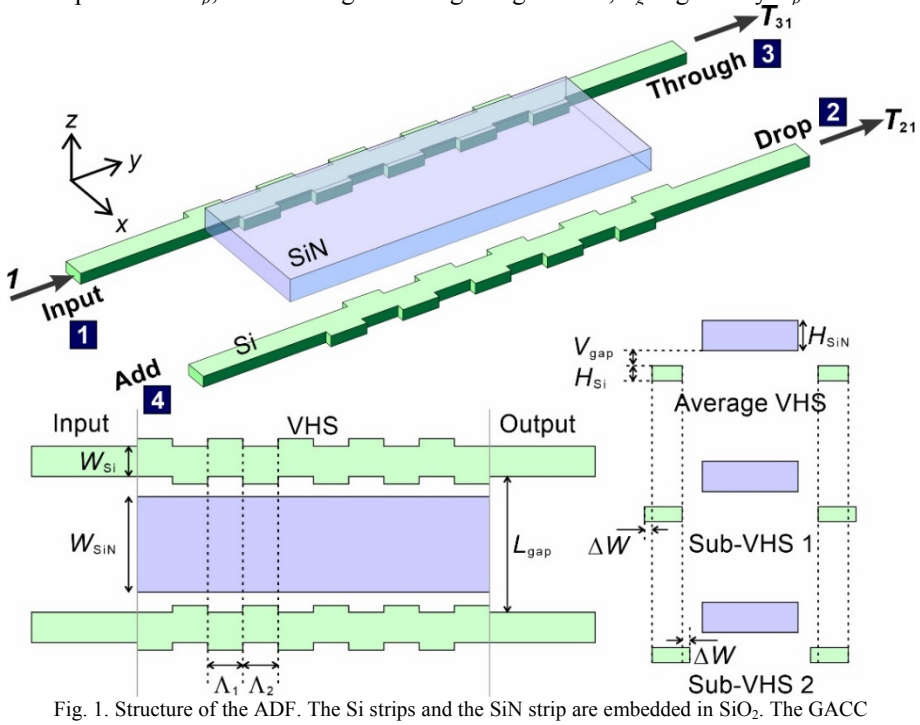

Fig. 1. Structure of the ADF. The Si strips and the SiN strip are embedded in SiO_2. The GACC is achieved in the VHS by periodically modulating the widths of the Si strips. The VHS can be considered as the periodic stack of sub-VHSs 1 and 2. The average VHS means the VHS without the width modulation. In other words, the average VHS has the Si strips of width W_{Si}.

The VHS supports even and odd TE and transverse-magnetic (TM) modes which are quite similar to the supermodes of just two parallel Si strip waveguides. The VHS also supports other modes confined mainly in the SiN strip. As L_{gap} increases, coupling between the Si strip waveguides becomes weaker, and the even and odd TE (TM) modes, represented by TE_{ev} and TE_{od} (TM_{ev} and TM_{od}), eventually become degenerate. In this regard, L_{gap} is chosen to be 2 μm such that TE_{ev} and TE_{od} are almost degenerate, which means that the difference between the effective indices of TE_{ev} and TE_{od} is smaller than 10^{-7}. Such a choice of L_{gap} is advantageous since fabrication of the two Si strip waveguides does not suffer from the proximity effect. In addition, much less effort is required to separate further the two Si strip waveguides when the ADF is integrated with other devices. The fundamental TE mode of the input port is evenly split into TE_{ev} and TE_{od} at the interface between the input section and the VHS with negligible loss. While they are traveling with almost the same propagation

Optics EXPRESS

constants in the VHS, there is the GACC between TE_{ev} and the lowest-order TE mode mainly confined in the SiN strip, which is denoted by TE_{N0}, at a wavelength λ_c. However, the grating affects insignificantly TE_{od}. N_p is determined such that TE_{ev} is completely coupled to TE_{N0} in the middle of the VHS. Then, TE_{N0} is completely coupled back to TE_{ev} at the end of the VHS, TE_{ev} and TE_{od} have a phase difference of π, and they are superposed to be the fundamental TE mode of the drop port. Since TE_{N0} is well confined in the SiN strip, its effective index does not change rapidly with a wavelength. This makes the bandwidth of the coupling small. At wavelengths distant from the coupling wavelength λ_c, the coupling is ineffective, there is no coupling-induced phase difference, and the superposition of TE_{ev} and TE_{od} results in the fundamental TE mode of the through port.

The ADF is analyzed and designed by using MODE Solutions of Lumerical Inc., which has the finite-difference eigenmode (FDE) solver and the bi-directional eigenmode expansion (EME) solver. The EME solver calculates wave propagation in a device for a given incident wave, and the transmissions of the ADF from the input port to the drop and through ports, T_{21} and T_{31} are accurately calculated by using it. When the FDE solver is used for mode analysis of the VHS, the VHS is surrounded by perfect electric conductor boundaries for fast simulation. When the EME solver is used, the ADF is surrounded by perfectly-matched-layer boundaries. The locations of the boundaries except the bottom boundary and mesh dimensions are determined to make simulation results converge. The bottom boundary is located 3 μm below the bottom of the Si strips to emulate 3-μm-thick buried oxide on a Si substrate. For the refractive indices of Si and SiO_2, the Lorentz model is used. In the case of SiN, its refractive index in [22] is used. At a wavelength of 1.55 μm, the refractive indices of Si, SiO_2, and SiN are 3.4734, 1.4433, and 2.0192, respectively.

Design of the ADF requires calculations of Λ and L_g. There are three methods of calculating Λ and L_g. The simplest method (hereafter called method 1) is to use the FDE solver in conjunction with the coupled-mode theory. The expressions of the drop-port transmission T_{21} and the through-port transmission T_{31} can be derived from the coupled-mode theory (see Appendices), which are given by

$$T_{21} = \frac{1}{4}\left[\cos(sy) - \cos(\delta y)\right]^2 + \frac{1}{4}\left[\frac{\delta}{s}\sin(sy) - \sin(\delta y)\right]^2, \quad (1)$$

$$T_{31} = \frac{1}{4}\left[\cos(sy) + \cos(\delta y)\right]^2 + \frac{1}{4}\left[\frac{\delta}{s}\sin(sy) + \sin(\delta y)\right]^2, \quad (2)$$

where $\delta = \pi\left(n_{ev,a}/\lambda - n_{N0,a}/\lambda - 1/\Lambda\right)$ and $s^2 = \kappa^2 + \delta^2$. λ is the free-space wavelength, and $n_{ev,a}$ and $n_{N0,a}$ represent the effective indices of TE_{ev} (the even TE mode confined in the Si strips) and TE_{N0} (the lowest-order TE mode mainly confined in the SiN strip) of the average VHS, respectively. κ is the coupling coefficient between TE_{ev} and the TE_{N0}. $T_{21} = 1$ and $T_{31} = 0$ if $\delta = 0$ and $\kappa y = \pi$. Therefore, $\Lambda = \lambda_c / \left(n_{ev,a} - n_{N0,a}\right)$, and $L_g = \pi/\kappa$. The expression of the 3-dB bandwidth $\Delta\lambda_{1/2}$ can be derived from Eq. (1) (see Appendices), which is given by

$$\Delta\lambda_{1/2} = 1.093\lambda_c^2 / (L_g \Delta n_g), \quad (3)$$

where Δn_g is the difference between the group indices of TE_{ev} and TE_{N0}.

The intermediate method of calculating Λ and L_g (hereafter called method 2) is to use the eigenmode solver and the transfer matrix approach [23], which is based on repetitive mode-matching and propagation of just forward-going TE_{ev} and TE_{N0} in the vertical hybrid structure. When an operation between mode a and mode b, $\langle a \mid b \rangle$ is defined by $\langle a \mid b \rangle = \frac{1}{2}\int \mathbf{E}_a \times \mathbf{H}_b^* \cdot \mathbf{x} ds$, where $\mathbf{E}_a$ and $\mathbf{H}_b$ are the electric field of mode a and the magnetic

Optics EXPRESS

field of mode *b*, respectively, the transmission coefficient $t_{(n,j)(m,i)}$ at the interface between sub-VHSs *i* and *j* is given by

$$t_{(n,j)(m,i)} = \frac{\langle (m,i) | (n,j) \rangle}{\sqrt{\langle (m,i) | (m,i) \rangle \langle (n,j) | (n,j) \rangle}}. \quad (4)$$

In Eq. (4), *m* and *n* correspond to 'ev' or 'N0', and *i* and *j* are equal to 1 or 2. When the length of sub-VHS *i*, $\Lambda_i = \frac{1}{2}\lambda_c / \left(n_{\mathrm{ev},i} - n_{\mathrm{N0},i}\right)$ for *i* = 1 and 2, where $n_{\mathrm{ev},i}$ and $n_{\mathrm{N0},i}$ represent the effective indices of $\mathrm{TE_{ev}}$ and $\mathrm{TE_{N0}}$ of sub-VHS *i*, respectively, the number of periods, N_p is given by

$$N_p = \left[\mathrm{sgn}(\phi)\pi - \alpha\right] / \phi, \quad (5)$$

where $\alpha = \sin^{-1}\left[(t_3 - t_1)/(2t_2)\right]$, $\phi = \tan^{-1}\left[2t_2 \cos\alpha / (t_3 + t_1)\right]$, $t_1 = t^2_{(\mathrm{ev},1)(\mathrm{ev},2)} - t^2_{(\mathrm{ev},1)(\mathrm{N0},2)}$, $t_2 = t_{(\mathrm{ev},1)(\mathrm{ev},2)} t_{(\mathrm{N0},1)(\mathrm{ev},2)} - t_{(\mathrm{ev},1)(\mathrm{N0},2)} t_{(\mathrm{N0},1)(\mathrm{N0},2)}$, and $t_3 = t^2_{(\mathrm{N0},1)(\mathrm{N0},2)} - t^2_{(\mathrm{N0},1)(\mathrm{ev},2)}$ [23]. Usually, since $|t_1| \approx |t_3| \approx 1$ and $|t_2| \ll 1$, $N_p \approx \pi / |t_2|$.

The most accurate, numerical method (hereafter called method 3) is to use the EME solver, but its workload is quite heavy since it requires sufficiently many modes of each constituent waveguide in a structure to be considered for simulation. Λ and L_g are found by calculating T_{21} for various values of Λ_1, Λ_2, and N_p and determining their values for which T_{21} is maximized. When method 3 is used, 20 modes of each uniform region of the ADF (*i.e.*, the input and output sections and the sub-VHSs) are considered for the calculation. The accuracy of methods 1 and 2 is compared with that of method 3 below.

The electric field profiles of the modes of the average VHS are shown in Fig. 2(a). They were calculated at a wavelength of 1.55 μm for W_{SiN} = 1.4 μm, H_{SiN} = 500 nm, and V_{gap} = 220 nm by using the eigenmode solver. In addition to $\mathrm{TE_{ev}}$, $\mathrm{TE_{od}}$ (the odd TE mode confined in the Si strips), and $\mathrm{TE_{N0}}$, the second-lowest-order TE mode mainly confined in the SiN strip exists, and it is represented by $\mathrm{TE_{N1}}$. The design of the ADF is to determine the values of W_{SiN}, H_{SiN}, V_{gap}, and Δ*W* to make the 3-dB bandwidth of the ADF smaller than 1.6 nm and the length of the grating section, L_g equal to about 1 mm. The target value of L_g is similar to the grating lengths of ADFs based on contra-directional coupling which have a 3-dB bandwidth of ~1 nm [3,7,8,12]. By referring to the previous vertical hybrid structures in [17–19], H_{SiN} is chosen between 400 nm and 600 nm, and V_{gap} is chosen between 150 nm and 220 nm. The values of Λ and N_p, which were calculated by using methods 1, 2, and 3, are shown in Fig. 2(b) to compare the accuracy of the methods. In the calculation, H_{SiN} = 500 nm, V_{gap} = 185 nm, Δ*W* = 20 nm, and λ_c = 1.55 μm. The values of Λ and N_p from method 1 based on the coupled-mode theory are significantly different from those from method 3 using the exact numerical analysis while the values of Λ and N_p from method 2 based on the transfer matrix approach are quite similar to those from method 3. The dominant component of the electric field of a TE mode is significantly discontinuous across the sidewalls of the Si strips. This causes the coupled-mode theory to yield the erroneous results, and method 1 is inaccurate. However, method 2 can determine accurately but efficiently Λ and N_p. Interestingly, as shown later, the transmission spectra calculated by using Eqs. (1) and (2) fit well those calculated by using method 3 if κ in Eqs. (1) and (2) is given by $\kappa = \pi / (N_p \Lambda)$ with N_p and Λ obtained from method 2. Therefore, the efficient analysis method for the design is to (1) use method 2 to determine Λ and L_g, (2) use Eqs. (1)–(3) to estimate T_{21}, T_{31}, and $\Delta\lambda_{1/2}$, and (3) use method 3 to refine Λ and L_g.

Λ and L_g were calculated as functions of W_{SiN} for various values of H_{SiN} and V_{gap} by using method 2. In addition, the 3-dB bandwidth $\Delta\lambda_{1/2}$ was also calculated by using Eq. (3). The results are shown in Figs. 2(c)–2(e). In all the calculations, the width modulation Δ*W* is 20 nm, and the coupling wavelength λ_c is 1.55 μm. As either W_{SiN} or H_{SiN} increases, the effective

Optics EXPRESS

index of TE_{N0} increases, and TE_{N0} is more strongly confined in the SiN strip. Therefore, Λ increases with W_{SiN} or H_{SiN}, and L_g increases with H_{SiN}. However, as W_{SiN} increases or V_{gap} decreases, the overlap between TE_{ev} and TE_{N0} increases, and hence L_g decreases. Since the change in the group index difference Δn_g depending on the parameters is smaller than that in L_g, the 3-dB bandwidth is almost inversely proportional to L_g. When H_{SiN} = 600 nm, synchronous coupling between TM_{od} (the odd TM mode confined in the Si strips) and TE_{N0} of the sub-VHSs happens for W_{SiN} between 1.26 μm and 1.3 μm, and the coupling between TE_{ev} and TE_{N0} becomes complicated. Hence, the values of W_{SiN} in this interval, which is denoted by the boxes in the figures, are excluded. Overall, the design goal of $\Delta\lambda_{1/2} < 1.6$ nm and $L_g \approx 1$ mm is achieved if H_{SiN} = 500 nm. Actually, the goal can be also achieved for H_{SiN} = 400 nm (600 nm) if ΔW is decreased below ~15 nm (increased above ~27 nm). This means that a variety of values of the parameters can be used, but, as an example, the characteristics of the ADF with W_{SiN} = 1.4 μm, H_{SiN} = 500 nm, V_{gap} = 220 nm, and ΔW = 20 nm are discussed in depth hereafter.

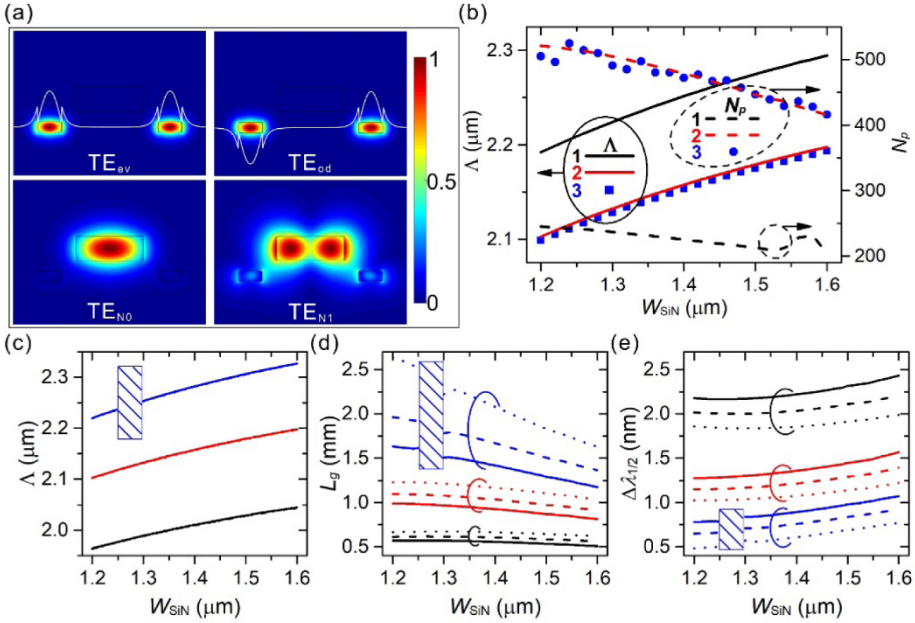

Fig. 2. Analysis results for the design of the ADF. (a) Electric field profiles of TE_{ev}, TE_{od}, TE_{N0}, and TE_{N1}. (b) Comparison of the results obtained from methods 1, 2, and 3, which are colored black, red, and blue, respectively. The solid (Λ) and dashed (N_p) curves were obtained from methods 1 and 2. The squares for Λ and the circles for N_p were obtained from method 3. (c) Dependence of Λ on W_{SiN}. (d) Dependence of L_g on W_{SiN}. (e) Dependence of the 3-dB bandwidth $\Delta\lambda_{1/2}$ on W_{SiN}. In (c)–(e), the curves for H_{SiN} = 400, 500, and 600 nm are colored black, red, and blue, respectively. The solid, dashed, and dotted curves show the dependences for V_{gap} = 150, 185, and 220 nm, respectively. The boxes show the interval of W_{SiN} for which synchronous coupling between TM_{od} and TE_{N0} of the sub-VHSs happens.

3. Characteristics of the ADF

For the ADF with W_{SiN} = 1.4 μm, H_{SiN} = 500 nm, and V_{gap} = 220 nm, the dependences of $\Delta\lambda_{1/2}$ and L_g on ΔW were calculated and they are shown in Fig. 3(a). As ΔW increases from 10 nm to 40 nm, $\Delta\lambda_{1/2}$ increases from 0.51 nm to 2.74 nm, and L_g decreases from 2.47 mm to 0.46 mm. Since the actual width of the Si strips of the sub-VHSs increases by ΔW, Λ decreases with increasing ΔW [see the inset of Fig. 3(a)]. The larger ΔW is, the stronger perturbation is caused by the grating. Consequently, the results from method 2 deviate more from those from method 3 for large values of ΔW. However, it is intriguing that L_g is still well anticipated by using method 2 with the formula $N_p = \pi / |t_2|$. The spectra of the drop-port transmission T_{21}

Optics EXPRESS

and the through-port transmission T_{31}, which were calculated by using method 3, are shown in Fig. 3(b). In the calculation, ΔW = 20 nm, Λ = 2.1525 μm, $\Lambda_1 = \Lambda_2$, and N_p = 524 (*i.e.*, L_g = 1.13 mm). The 3-dB bandwidth extracted from the T_{21} spectrum is 1.16 nm, which is almost equal to the value found in Fig. 2(e). The transmission spectra calculated with Eqs. (1) and (2) are also shown and they fit well those from method 3 as mentioned above. The parameters of Eqs. (1) and (2) except κ are obtained from method 1, but κ is obtained from method 2 with the formula $\kappa = \pi / L_g$. The 3-dB bandwidth and grating region length of this ADF are similar to those of the ADFs using an asymmetric directional coupler in [3,7,8]. T_{21} at λ_c (1.55 μm) is −0.02 dB, and T_{31} at λ_c, which corresponds to transmission isolation at the through port, is −34.4 dB. This isolation is smaller than the calculated isolation of the ADF using an asymmetric directional coupler in [5]. The reflection from the input port at λ_c is −55.5 dB. At a wavelength of 1.5 μm, T_{21} and T_{31} are −46.2 dB and −0.037 dB, respectively. T_{21} at this wavelength corresponds to a crosstalk from the through port to the drop port, and it is much smaller than that in [5]. Since the grating of this ADF scatters insignificantly light, the reflection, the drop port loss, and the through port loss are very small in theory. This ADF is designed for TE polarization. In the case of TM polarization, the even and odd TM modes, TM_{ev} and TM_{od} are not degenerate due to weak confinement of the TM modes in the Si strips. The difference between their effective indices at 1.55 μm is 2.5 × 10^{-4}. If Λ and L_g are adjusted to 14.522 μm and 4.429 mm, respectively, T_{21} at λ_c is −0.12 dB, and T_{31} is −49.5 dB. However, the beat length between the TM modes is 6.2 mm, which is similar to L_g, and the beating between the TM modes makes the transmission spectra complicated.

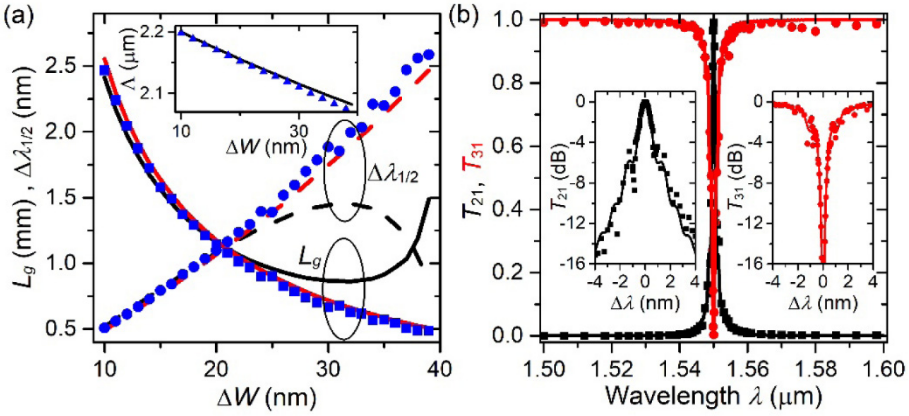

Fig. 3. Characteristics of the ADF. (a) Dependences of L_g and $\Delta\lambda_{1/2}$ on ΔW. The inset shows the dependence of Λ on ΔW. The solid and dashed curves were obtained from method 2; the symbols were obtained from method 3. The black curves were calculated by using Eq. (5); the red curves were calculated by using the approximate equation $N_p = \pi / |t_2|$. (b) Transmission spectra. The spectra of T_{21} and T_{31} are colored black and red, respectively. The symbols were obtained from method 3. The solid curves were calculated by using Eqs. (1) and (2). The insets show the spectra in dB in a narrow wavelength interval. $\Delta\lambda$ is wavelength detuning from λ_c = 1.55 μm. The minimum of T_{31} in the right inset is clamped to −16 dB for clear demonstration.

Since the VHS supports TE_{N1}, TE_{od} can be coupled to TE_{N1} via the grating. However, in the case of the above ADF, the coupling happens at a wavelength of 1.699 μm (see Appendices). Even coupling between TE_{od} and the lowest-order TM mode mainly confined in the SiN strip, TM_{N0} occurs at a wavelength of 1.6125 μm (see Appendices). As W_{SiN} increases, the coupling between TE_{od} and TE_{N1} exists at a wavelength closer to 1.6 μm. Moreover, coupling between TE_{ev} and TM_{od} and coupling between TE_{od} and TM_{ev} exist at wavelengths near 1.5 μm for a large value of W_{SiN} (*e.g.*, 2 μm) (see Appendices). Therefore, if just one channel needs to be dropped or added within the range of 1.5 μm to 1.6 μm, it is better not to make W_{SiN} large.

Optics EXPRESS

The values of W_{Si}, W_{SiN}, H_{SiN}, and V_{gap} of a realized ADF may deviate from the designed values, and the characteristics of the ADF, especially the coupling wavelength λ_c, change depending on those parameters. The changes in λ_c, $\Delta\lambda_c$ and T_{21} at λ_c were calculated as functions of W_{Si}, W_{SiN}, H_{SiN}, or V_{gap} by using method 3, and the calculation results are shown in Fig. 4. When X represents one of the parameters,

$$\frac{\partial\lambda_c}{\partial X} = \frac{\lambda_c}{\Delta n_g}\frac{\partial(n_{ev,1} - n_{N0,1})}{\partial X}. \tag{6}$$

Equation (6) is used to calculate the slopes of the straight lines which are fitted to the relations of $\Delta\lambda_c$ to the parameters. The slopes (in nm/nm) are 1.039, –0.0576, –0.334, and –0.0111 for W_{Si}, W_{SiN}, H_{SiN}, and V_{gap}, respectively. λ_c does not depend sensitively on W_{SiN} and V_{gap}, but it significantly depends on W_{Si}. To make the maximum change in λ_c smaller than half the channel spacing, namely 0.8 nm, the maximum changes in W_{Si}, W_{SiN}, H_{SiN}, and V_{gap} must be smaller than 0.77 nm, 14 nm, 2.4 nm, and 72 nm, respectively. The fabrication tolerance for W_{Si} is very small. As in Si photonic ring resonators, the ADF may be thermo-optically tuned to cancel out the influence of fabrication errors. Since T_{21} at λ_c is affected by V_{gap} as shown in Fig. 4(d), the change in V_{gap} has to be restricted to less than 10 nm. In addition to the four parameters, the period also needs to be considered. The change rate of λ_c with respect to Λ is estimated by $\partial\lambda_c/\partial\Lambda = (\lambda_c/\Lambda)^2/\Delta n_g$, which is equal to 0.248. According to calculation using method 3, the change rate is 0.246. Therefore, the change in Λ has to be smaller than 3.25 nm to make λ_c shift by less than 0.8 nm.

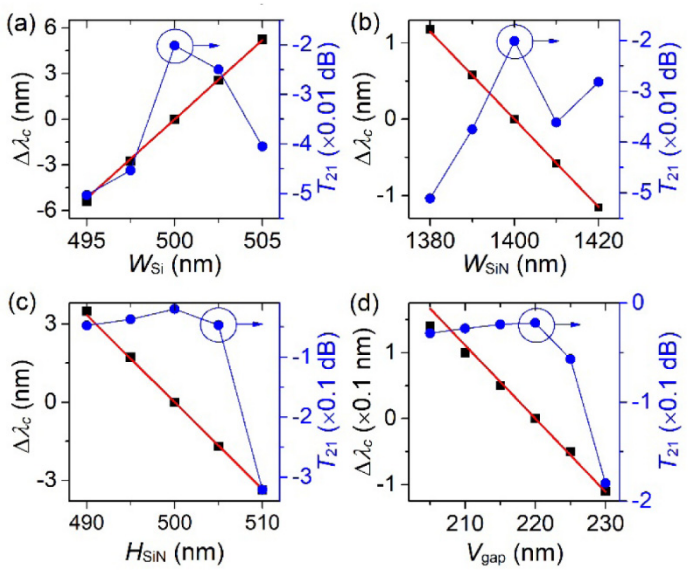

Fig. 4. Changes in λ_c and T_{21} at λ_c depending on (a) W_{Si}, (b) W_{SiN}, (c) H_{SiN}, and (d) V_{gap}. $\Delta\lambda_c$ means the change in λ_c. The squares for $\Delta\lambda_c$ and the circles for T_{21} at λ_c were obtained from method 3. The straight lines with the slope calculated with Eq. (6) are fitted to the squares.

The ADF is symmetric about the central vertical plane, and it is necessary to check how the characteristics of the ADF change if the symmetry is broken. Two cases are considered: the Si strips with different widths and the SiN strip displaced from the central position. First, the spectra of T_{21} and T_{31} in Figs. 5(a) and 5(b) were calculated under the assumption that the right Si strip is wider than the left one by 0.6 nm. This value corresponds to the upper bound of nonuniformity in a chip which is fabricated by using 193 nm optical lithography and dry etching [24]. The spectra slightly shift by 0.25 nm, and the maximum of T_{21} decreases to

Optics EXPRESS

0.553 as shown in Fig. 5(a). The minute difference between the widths of the Si strips seriously degrades the characteristics of the ADF. Gratings-assisted coupling among three different waveguides can be analyzed by using the coupled-mode theory (see Appendices), and the spectra obtained from the analysis are shown in Figs. 5(a) and 5(b). They show good agreement with the spectra calculated by using method 3. Next, the spectra of T_{21} and T_{31} were calculated under the assumption that the SiN strip is displaced by 12 nm from the central position. This value corresponds to the upper bound of layer-to-layer alignment accuracy [10]. The spectra in Figs. 5(c) and 5(d) are almost the same as those of the symmetric ADF in Fig. 3(b). This indicates that the ADF is quite tolerant to the asymmetry due to the displacement of the SiN strip. On one hand, the degradation due to the asymmetry in the Si strip width can be canceled out if the refractive index of the right (left) Si strip is slightly decreased (increased). When the refractive index decrease of the right Si strip with a width increase of 0.6 nm is 8.112×10^{-4}, the spectra becomes almost the same as those of the symmetric ADF (see Appendices). On the other hand, it is possible to deliberately make the Si strips have quite different widths. If the Si strips have two respective gratings with different periods and width modulations, which are chosen considering the width difference, the ADF with such Si strips and gratings functions like the symmetric ADF (see Appendices).

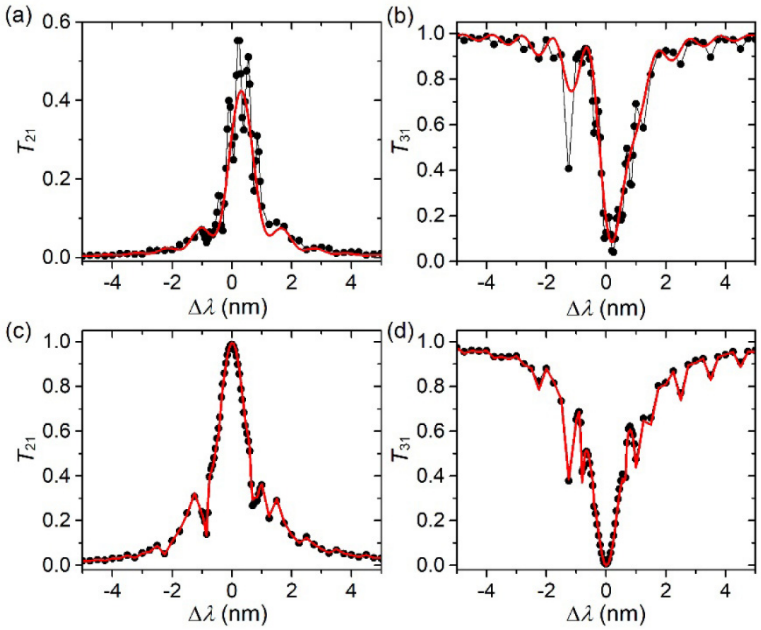

Fig. 5. Transmission spectra of the asymmetric ADF. $\Delta\lambda$ is wavelength detuning from λ_c = 1.55 μm. (a) and (b) were calculated in the case that the right Si strip is 0.6 nm wider than the left Si strip. (c) and (d) were calculated in the case that the SiN strip is displaced by 12 nm from the central position. The symbols were obtained from method 3. The solid curves in (a) and (b) were calculated by using the coupled-mode theory for three waveguides (see Appendices). The solid curves in (c) and (d) show the spectra of the symmetric ADF for comparison.

4. Nonvolatile switchable ADF

Switchable ADFs, which are a combination of an ADF and an optical switch, may simplify reconfigurable add drop multiplexers which are based on separate ADFs and optical switches [25]. Various switchable ADFs have been developed, and the thermo-optic effect is usually used for switching [26,27]. The state of a switchable ADF is temporarily maintained while electric power for switching is being consumed. The power consumption may be reduced if switchable ADFs are nonvolatile. The investigated ADF is a good platform for a nonvolatile

Optics EXPRESS

switchable ADF, which is made by placing a strip of an optical phase change material on the SiN strip as shown in Fig. 6(a). Optical phase change materials are in an amorphous state or in a crystalline state [28–30]. Phase transition between the amorphous and crystalline states is induced thermally or optically, and it results in a huge change in the refractive index or permittivity of an optical phase change material. Recently, a low-loss optical phase change material $Ge_2Sb_2Se_4Te_1$ (GSST) has been reported [31]. Amorphous GSST (a-GSST) has a small extinction coefficient of the order of 10^{-4} at a wavelength of 1.55 μm while the extinction coefficient of crystalline GSST (c-GSST) is about 0.42. The GSST strip, the width and height of which are W_{gsst} and H_{gsst}, respectively, is centered on the central vertical line and it is a distance G_{gap} above the SiN strip. The refractive indices and extinction coefficients of a-GSST and c-GSST are obtained from [31] and they are used to analyze the GSST-added ADF.

The electric field profiles of TE_{N0} in the cases of a-GSST and c-GSST are shown in Figs. 6(b) and 6(c), respectively. They were calculated at a wavelength of 1.55 μm for W_{gsst} = 300 nm, H_{gsst} = 50 nm, and G_{gap} = 100 nm. TE_{ev} and TE_{od} are hardly affected by the GSST strip. However, a small portion of the field of TE_{N0} is confined in the a-GSST strip, and TE_{N0} has a small propagation loss of 0.52 dB/cm. TE_{N0} becomes more confined in the c-GSST strip since the refractive index of c-GSST is larger than that of a-GSST. This strong confinement in the c-GSST strip makes the coupling coefficient between TE_{ev} and TE_{N0} much smaller than that in the case of a-GSST. Moreover, the propagation loss of TE_{N0} in the case of c-GSST increases to 9585 dB/cm while the real part of the effective index of TE_{N0} increases from 1.7655 to 1.7983. GACC between a lossless or low-loss mode and a high-loss mode is almost impossible if the attenuation coefficient of the high-loss mode is much larger than the coupling coefficient between the two modes regardless of phase matching between the two modes [32]. The attenuation coefficient of TE_{N0} in the case of c-GSST is of the order of 10^{-1} μm^{-1}, but the coupling coefficient even in the case of a-GSST is of the order of 10^{-3} μm^{-1}. Therefore, the GACC in the ADF does not exist and the ADF is switched off when the GSST strip becomes crystalline. This means that the fundamental TE mode of the input port goes to the through port without being dropped to the drop port.

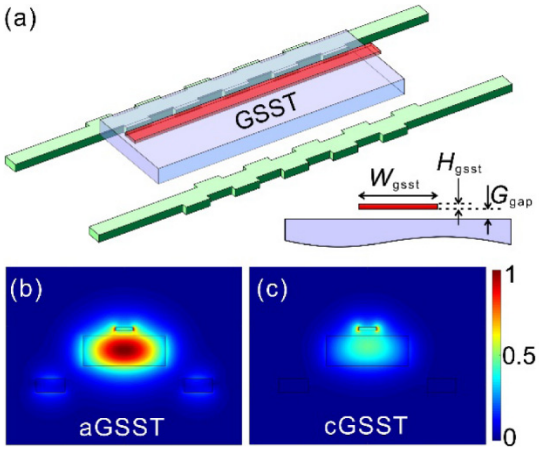

Fig. 6. Nonvolatile switchable ADF. (a) Schematic diagram of its structure. (b) Electric field profile of TE_{N0} in the case of a-GSST. (c) Electric field profile of TE_{N0} in the case of c-GSST.

The influences of W_{gsst} and G_{gap} on the ADF were calculated by using method 3, and Λ, N_p, T_{21} at λ_c in the case of a-GSST, and T_{31} at λ_c in the case of c-GSST are shown as functions of W_{gsst} for G_{gap} = 50, 100, and 150 nm in Fig. 7. In the calculation, H_{gsst} was set at 50 nm, and the values of the other parameters were the same as those of the above ADF without the GSST strip. As W_{gsst} increases or G_{gap} decreases, TE_{N0} is more strongly confined in the GSST

Optics EXPRESS

strip, and hence both the real and imaginary parts of the effective index of TE_{N0} increase. This explains why Λ and N_p increase and T_{21} at λ_c in the case of a-GSST generally decreases as W_{gsst} increases or G_{gap} decreases. In the case of c-GSST, the larger W_{gsst} is or the smaller G_{gap} is, the more suppressed is the coupling between TE_{ev} and TE_{N0}. Therefore, T_{31} at λ_c increases with increasing W_{gsst} or decreasing G_{gap}. The spectra of T_{21} and T_{31} in Fig. 8 were calculated for W_{gsst} = 300 nm and G_{gap} = 100 nm. In this case, Λ = 2.1918 μm, N_p = 598, and L_g = 1.31 mm. The spectra in the case of a-GSST are similar to those of the ADF without the GSST strip. In the case of c-GSST, $T_{21} \approx 0$, and $T_{31} \approx 1$ in the range of 1.5 μm to 1.6 μm. The phase transition of GSST decreases T_{21} at λ_c from −0.0455 dB to −34.8 dB and it increases T_{31} at λ_c from −30.2 dB to −0.189 dB.

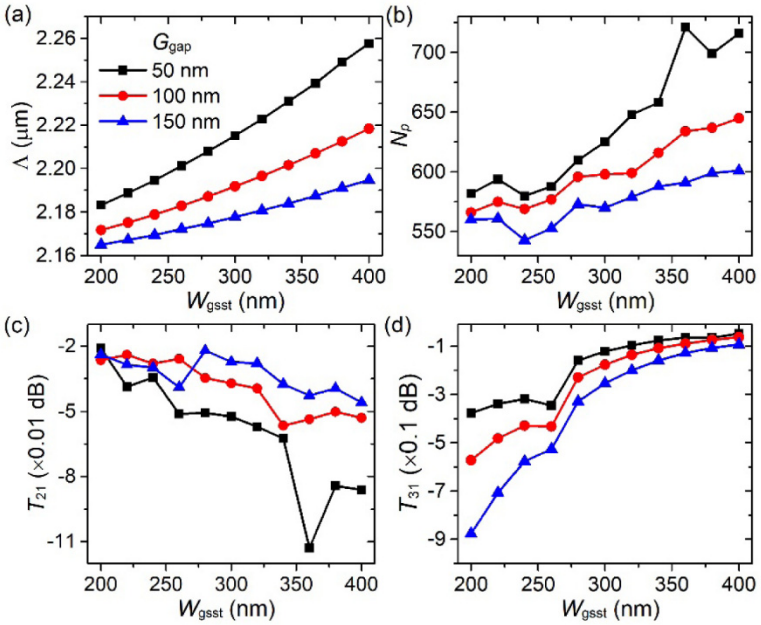

Fig. 7. Influences of W_{gsst} and G_{gap} on the nonvolatile switchable ADF. The panels show how (a) Λ, (b) N_p, (c) T_{21} at λ_c in the case of a-GSST, and (d) T_{31} at λ_c in the case of c-GSST depend on W_{gsst} for G_{gap} = 50 (black squares), 100 (red circles), and 150 (blue triangles) nm.

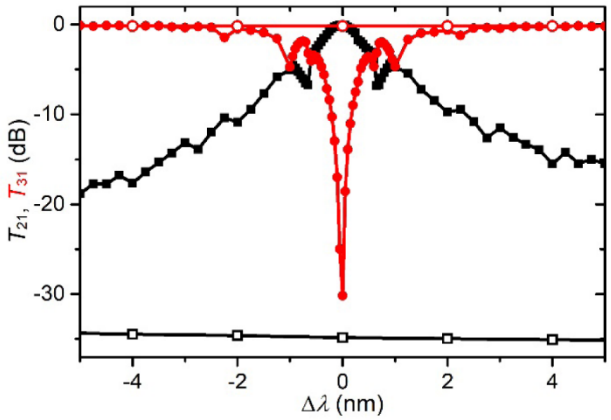

Fig. 8. Spectra of T_{21} and T_{31} in the case of a-GSST (closed symbols) and in the case of c-GSST (open symbols). $\Delta\lambda$ is wavelength detuning from λ_c = 1.55 μm. The solid lines are guides for the eye.

Optics EXPRESS

5. Conclusion

The ADF using the GACC in the VHS has been theoretically investigated. In doing so, the efficient and accurate analysis method for the design of the ADF has been presented. The investigated ADF has a 3-dB bandwidth of 1.16 nm and a grating length of 1.13 mm, which are similar to those of ADFs based on contra-directional coupling. However, it has the advantages from the perspective of ease of fabrication as compared to ADFs based on contra-directional coupling: the unnecessity of two Si waveguides in close proximity, the use of grating teeth much longer than the resolution of deep UV lithography, and the unnecessity of additional waveguides redirecting the drop and add ports, 3-dB couplers, and adiabatic mode converters. Actually, the ease of fabrication is obtained at the cost of additional fabrication processes to realize VHSs such as planarization and SiN strip formation. Since VHSs have been realized, the ADF could be fabricated as designed. Either symmetric or asymmetric fabrication errors in the widths of the Si strips most significantly affect the ADF characteristics. It has been demonstrated that the influence of such fabrication errors can be cancelled out by tuning the refractive indices of the Si strips. As one application of the ADF, the nonvolatile switchable ADF has been investigated. The nonvolatile switching with an extinction ratio larger than 30 dB is enabled by the phase transition of the GSST strip which is simply added atop the ADF. The ADF is expected to play a key role in optical interconnection based on DWDM.

This research was supported by Basic Science Research Program through the National Research Foundation of Korea (NRF) funded by the Ministry of Science, ICT & Future Planning (NRF-2017R1A2B4007143).

Appendices

Group index difference of two in-plane Si waveguides

Two cases can be considered: one is coupling between two Si strip waveguides with different widths, and the other is coupling between a Si strip waveguide and a Si slot waveguide. In the first case, the difference between the group indices of the two Si strip waveguides is 0.361 if the widths are 500 nm and 1000 nm. In the second case, the Si strip waveguide is 500 nm wide, the rails of the Si slot waveguide are 250 nm wide, and the slot is 100 nm wide. Then, the difference between the group indices of the two waveguides is 1.001. This is more than two times smaller than the group index difference between TE_{ev} and TE_{N0}.

Derivations of Eqs. (1)–(3)

The fundamental TE mode of the left Si waveguide in the input section has the transversal electric field $\mathbf{E}_{\text{left}}(x,z)$. It is normalized such that $\frac{1}{2}\iint \mathbf{E}_{\text{left}}(x,z)\times\mathbf{H}^{*}_{\text{left}}(x,z)\cdot \text{y}dxdz = 1\,\text{W}$, where $\mathbf{H}_{\text{left}}(x,z)$ is the transversal magnetic field of the fundamental TE mode. The fundamental TE mode of the right Si waveguide also has the normalized transversal electric field $\mathbf{E}_{\text{right}}(x,z)$. If $\mathbf{E}_{\text{ev}}(x,z)$ and $\mathbf{E}_{\text{od}}(x,z)$ represent the normalized transversal electric fields of TE_{ev} and TE_{od}, respectively, then

$$\mathbf{E}_{\text{ev}} = \frac{1}{\sqrt{2}}\mathbf{E}_{\text{left}} + \frac{1}{\sqrt{2}}\mathbf{E}_{\text{right}}, \tag{7}$$

$$\mathbf{E}_{\text{od}} = -\frac{1}{\sqrt{2}}\mathbf{E}_{\text{left}} + \frac{1}{\sqrt{2}}\mathbf{E}_{\text{right}}. \tag{8}$$

The equalities in Eqs. (7) and (8) are almost exact since the two Si strips of the VHS are sufficiently separated. When the fundamental TE mode of the left Si waveguide is incident on

Optics EXPRESS

the VHS at $y = 0$, TE_{ev} with an amplitude of $1/\sqrt{2}$ and TE_{od} with an amplitude of $-1/\sqrt{2}$ are excited. According to the well-known expressions from the coupled-mode theory for two waveguides, the transversal electric field $\mathbf{E}_{Si}$ which is mainly confined in the Si strips at $y = L_g$ is given by

$$\mathbf{E}_{Si} = \frac{1}{\sqrt{2}}\exp(i\beta_{ev}L_g)\exp(-i\delta L_g)\times\left[\cos(sL_g)+\frac{i\delta}{s}\sin(sL_g)\right]\mathbf{E}_{ev} - \frac{1}{\sqrt{2}}\exp(i\beta_{od}L_g)\mathbf{E}_{od}, \quad (9)$$

where β_{ev} and β_{od} are the propagation constants of TE_{ev} and TE_{od}, respectively. When β_{N0} is the propagation constant of TE_{N0}, the phase mismatch factor δ is given by $\delta = (\beta_{ev} - \beta_{N0} - 2\pi/\Lambda)/2$. When $\Lambda_1 = \Lambda_2 = \Lambda/2$, the coupling coefficient κ between TE_{ev} and TE_{N0} is given by

$$\kappa = \left|\kappa_{out} - \kappa_{in}\right|/\pi, \quad (10a)$$

$$\kappa_{\substack{out\\in}} = \frac{\pi}{2\eta_0\lambda}\left(n_{Si}^2 - n_{SiO}^2\right)\times\left(\iint_{\substack{out\\in}}\mathbf{E}_{ev}^{*}\cdot\mathbf{E}_{N0}dxdz + \frac{n_{SiO}^2}{n_{Si}^2}\iint_{\substack{out\\in}}E_{ev,y}^{*}\cdot E_{N0,y}dxdz\right), \quad (10b)$$

where λ, η_0, n_{Si}, and n_{SiO} represent the free space wavelength, the intrinsic impedance in vacuum, the refractive index of Si, and that of SiO_2, respectively. $E_{ev,y}$ and $E_{N0,y}$ are the longitudinal components of the normalized electric fields of TE_{ev} and TE_{N0}, respectively; $\mathbf{E}_{N0}$ is the normalized tangential electric field of TE_{N0}. The integration is carried out in the region where the Si strips are widened outwards or inwards by ΔW. In Eq. (9), $s = \sqrt{\kappa^2 + \delta^2}$. Since TE_{ev} and TE_{od} are degenerate, $\beta_{ev} = \beta_{od}$, and Eqs. (7)–(9) give

$$\begin{aligned} T_{21} &= \frac{1}{4}\left|\exp(-i\delta L_g)\left[\cos(sL_g)+\frac{i\delta}{s}\sin(sL_g)\right]-1\right|^2 \\ &= \frac{1}{4}\left[\cos(sL_g)-\cos(\delta L_g)\right]^2 + \frac{1}{4}\left[\frac{\delta}{s}\sin(sL_g)-\sin(\delta L_g)\right]^2, \end{aligned} \quad (11a)$$

$$\begin{aligned} T_{31} &= \frac{1}{4}\left|\exp(-i\delta L_g)\left[\cos(sL_g)+\frac{i\delta}{s}\sin(sL_g)\right]+1\right|^2 \\ &= \frac{1}{4}\left[\cos(sL_g)+\cos(\delta L_g)\right]^2 + \frac{1}{4}\left[\frac{\delta}{s}\sin(sL_g)+\sin(\delta L_g)\right]^2. \end{aligned} \quad (11b)$$

To derive Eq. (3), it is assumed that $\delta = \alpha\kappa$. Then, $T_{21} = 0.5$ if

$$2 = \frac{1}{4}\left[\cos\left(\pi\sqrt{1+\alpha^2}\right)-\cos(\pi\alpha)\right]^2 + \frac{1}{4}\left[\frac{\alpha}{\sqrt{1+\alpha^2}}\sin\left(\pi\sqrt{1+\alpha^2}\right)-\sin(\pi\alpha)\right]^2. \quad (12)$$

Equation (12) is solved for α, and $\alpha = 0.5466$. From the definition of δ,

$$\Delta\delta = \alpha\kappa = \pi\Delta\left(\frac{n_{ev,a}-n_{N0,a}}{\lambda}\right) \simeq -\frac{\pi}{2}\Delta\lambda_{1/2}\frac{\Delta n_g}{\lambda_c^2}. \quad (13)$$

In consequence, $\Delta\lambda_{1/2} = 1.093\lambda_c^2/(L_g\Delta n_g)$.

Optics EXPRESS

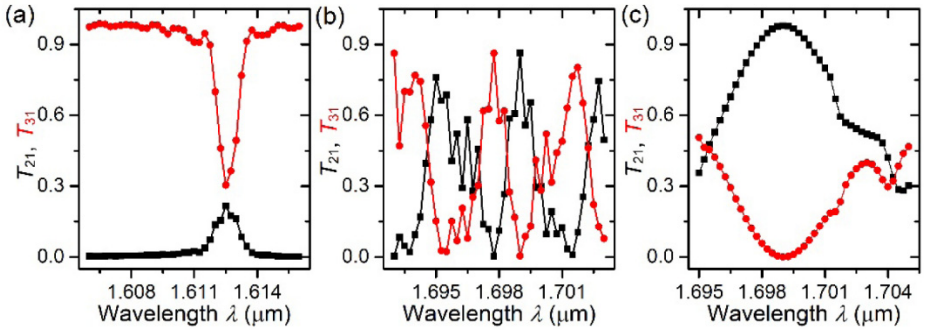

Fig. 9. T_{21} and T_{31} spectra of the ADF with W_{SiN} = 1.4 μm. (a) Coupling between TE_{od} and TM_{N0}. (b) Coupling between TE_{od} and TE_{N1}. (c) Coupling between TE_{od} and TE_{N1} when N_p is reduced to 100.

Additional couplings occurring in the investigated ADF

The investigated ADF (with W_{SiN} = 1.4 μm, H_{SiN} = 500 nm, V_{gap} = 220 nm, Λ = 2.1525 μm, and N_p = 524) has the coupling between TE_{od} and TM_{N0} at a wavelength of 1.6125 μm and the coupling between TE_{od} and TE_{N1} at a wavelength of 1.699 μm. This can be confirmed from the spectra of T_{21} and T_{31} in Fig. 9. Since the coupling between TE_{od} and TE_{N1} is much stronger than that between TE_{ev} and TE_{N0}, N_p needs to be reduced. Figure 9(c) shows the spectra for N_p = 100. In this case, T_{21} and T_{31} go to 0 and 1, respectively, at 1.699 μm. When W_{SiN} is increased to 1.7 μm, the desired coupling between TE_{ev} and TE_{N0} exists at 1.55 μm if Λ and N_p are adjusted to be 2.2084 μm and 440, respectively. Then, the coupling between TE_{od} and TM_{N0} exists at ~1.6205 μm, and the coupling between TE_{od} and TE_{N1} exists at ~1.659 μm as shown in Figs. 10(a) and 10(b). When W_{SiN} is increased to 2.0 μm, the desired coupling between TE_{ev} and TE_{N0} exists at 1.55 μm if Λ and N_p are adjusted to be 2.2445 μm and 369, respectively. As shown in Fig. 10(c), the coupling between TE_{od} and TM_{N0} and that between TE_{od} and TE_{N1} happen around 1.629 μm in a complicated way. Moreover, the coupling between TE_{ev} and TM_{od} and that between TE_{od} and TM_{ev} happen at ~1.524 μm as shown in Fig. 10(d).

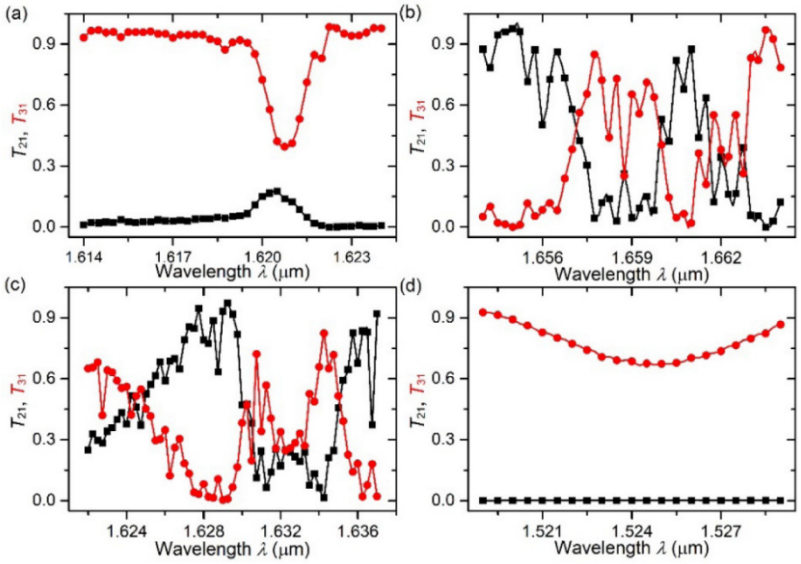

Fig. 10. T_{21} and T_{31} spectra of the ADF. (a) Coupling between TE_{od} and TM_{N0} for W_{SiN} = 1.7 μm. (b) Coupling between TE_{od} and TE_{N1} for W_{SiN} = 1.7 μm. (c) Coupling between TE_{od} and TM_{N0} and that between TE_{od} and TE_{N1} for W_{SiN} = 2.0 μm. (d) Coupling between TE_{ev} and TM_{od} and that between TE_{od} and TM_{ev} for W_{SiN} = 2.0 μm.

Optics EXPRESS

Analysis of gratings-assisted coupling among three waveguide modes

There is a waveguide supporting three waveguide modes propagating in the y direction. Modes 1 and 3 are coupled to each other via a grating with a period Λ_{13}, and Modes 2 and 3 are coupled to each other via a grating with a period Λ_{23}. Then, the coupled-mode equations for the amplitudes of modes 1, 2, and 3 are

$$da_1 / dy = i\kappa_{13} a_3 \exp(-i2\delta_{13} y), \tag{14a}$$

$$da_2 / dy = i\kappa_{23} a_3 \exp(-i2\delta_{23} y), \tag{14b}$$

$$da_3 / dy = i\kappa_{13}^* a_1 \exp(i2\delta_{13} y) + i\kappa_{23}^* a_2 \exp(i2\delta_{23} y), \tag{14c}$$

where $\delta_{j3} = (\beta_j - \beta_3 - 2\pi / \Lambda_{j3}) / 2$ for j = 1 and 2 and β_j is the propagation constant of mode j for j = 1 to 3. κ_{j3} is the coupling coefficient between modes j and 3 for j = 1 and 2. If a_1, a_2, and a_3 are substituted by $A_1 \exp(-i\delta_d y)$, $A_2 \exp(i\delta_d y)$, and $A_3 \exp(i\delta_s y)$, where $\delta_d = \delta_{13} - \delta_{23}$ and $\delta_s = \delta_{13} + \delta_{23}$, Eq. (14) becomes

$$\frac{d}{dy}\begin{bmatrix} A_1 \\ A_2 \\ A_3 \end{bmatrix} = i\begin{bmatrix} \delta_d & 0 & \kappa_{13} \\ 0 & -\delta_d & \kappa_{23} \\ \kappa_{13}^* & \kappa_{23}^* & -\delta_s \end{bmatrix}\begin{bmatrix} A_1 \\ A_2 \\ A_3 \end{bmatrix}, \tag{15}$$

and Eq. (15) has a general solution $\mathbf{A} = \mathrm{v}\exp(i\zeta y)$, where $\mathbf{A}$ is the column vector in Eq. (15). ζ and $\mathbf{v}$ are the eigenvalue and eigenvector of the 3-by-3 matrix in Eq. (15), respectively, and ζ is given by a solution of

$$\zeta^3 + \delta_s \zeta^2 - (\kappa_{13}^2 + \kappa_{23}^2 + \delta_d^2)\zeta + (\kappa_{23}^2 - \kappa_{13}^2)\delta_d - \delta_d^2 \delta_s = 0. \tag{16}$$

The eigenvector $\mathbf{v}_j$ corresponding to the eigenvalue ζ_j is given by

$$\mathbf{v}_j = \begin{bmatrix} -\kappa_{13}(\delta_d + \zeta_j) \\ \kappa_{23}(\delta_d - \zeta_j) \\ \delta_d^2 - \zeta_j^2 \end{bmatrix}. \tag{17}$$

With the initial condition that $a_1(0) = 1$, $a_2(0) = 0$, and $a_3(0) = 0$, the solution of Eq. (14) is given by

$$\begin{bmatrix} a_1(y) \\ a_2(y) \\ a_3(y) \end{bmatrix} = \mathbf{D}_\delta \mathbf{V} \mathbf{D}_\zeta \mathbf{V}^{-1} \begin{bmatrix} a_1(0) \\ a_2(0) \\ a_3(0) \end{bmatrix}, \tag{18}$$

where $\mathbf{D}_\delta$ and $\mathbf{D}_\zeta$ are diagonal matrices and $\mathbf{V}$ is the matrix given by [$\mathbf{v}_1$ $\mathbf{v}_2$ $\mathbf{v}_3$]. The diagonal elements of $\mathbf{D}_\delta$ are $\exp(-i\delta_d y)$, $\exp(i\delta_d y)$, and $\exp(i\delta_s y)$. The diagonal elements of $\mathbf{D}_\zeta$ are $\exp(i\zeta_1 y)$, $\exp(i\zeta_2 y)$, and $\exp(i\zeta_3 y)$.

When this analysis is applied to the ADF, modes 1 and 2 correspond to the modes mainly confined in the left and right Si strips, respectively, and mode 3 corresponds to TE_{N0}. In other words, the tangential electric fields of modes 1 and 2 are given by $(\mathbf{E}_{ev} \mp \mathbf{E}_{od}) / \sqrt{2}$. Then, $\Lambda_{13} = \Lambda_{23} = \Lambda$, and $\delta_{13} = \delta_{23} = \delta$. Hence, $\delta_d = 0$, and $\delta_s = 2\delta$. It can be easily shown from

Optics EXPRESS

Eqs. (7), (9), and (10) that $\kappa_{13} = \kappa_{23} = \kappa/\sqrt{2}$. The solutions of Eq. (16) are $\zeta_1 = 0$, $\zeta_2 = -\delta + s$, and $\zeta_3 = -\delta - s$. From Eq. (18),

$$a_1(y) = \frac{1}{2}\left[1 + \exp(-i\delta y)\cos(sy) + i\frac{\delta}{s}\exp(-i\delta y)\sin(sy)\right], \tag{19a}$$

$$a_2(y) = \frac{1}{2}\left[-1 + \exp(-i\delta y)\cos(sy) + i\frac{\delta}{s}\exp(-i\delta y)\sin(sy)\right]. \tag{19b}$$

Since $|a_1(L_g)|^2 = T_{21}$ and $|a_2(L_g)|^2 = T_{31}$, consequently, Eq. (19) results in Eq. (5).

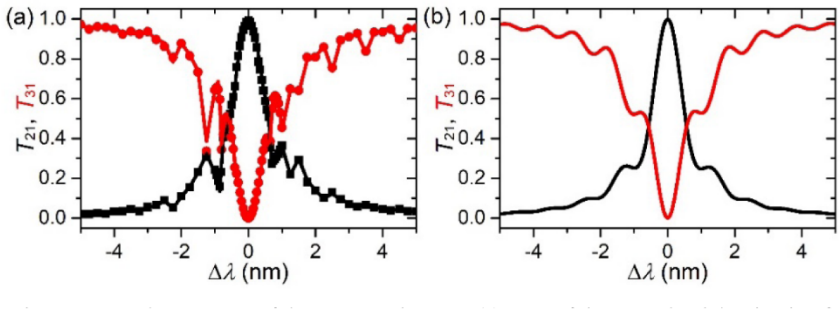

Fig. 11. T_{21} and T_{31} spectra of the asymmetric ADF. (a) Case of the ADF the right Si strip of which has a larger width and a smaller refractive index than the left Si strip. The symbols show its spectra calculated by using method 3. For comparison, the solid curves show the spectra of the symmetric ADF in Fig. 3(b). (b) Case of the truly asymmetric ADF which has the left Si strip of width 500 nm and the right Si strip of width 480 nm. The width change of the left Si strip is 20 nm, and that of the right Si strip is 22.7 nm. The spectra were calculated by using Eqs. (16)–(18). $\Delta\lambda$ is wavelength detuning from λ_c = 1.55 μm.

Asymmetric ADF

The T_{21} and T_{31} spectra in Fig. 5 were calculated by using Eqs. (16)–(18). For the calculation, β_1, β_2, and β_3 were obtained from mode analysis of the average VHS; method 2 was used to determine κ_{13} and κ_{23}.

As mentioned in the main text, the effect of the width difference between the two Si strips can be cancelled out by decreasing the refractive index of the right Si strip. The T_{21} and T_{31} spectra were calculated by using method 3 and they are shown in Fig. 11(a). They are almost the same as the spectra of the symmetric ADF in Fig. 3(b).

The truly asymmetric ADF which has the left Si strip of width 500 nm and the right Si strip of width 480 nm is analyzed (the other parameters except the width change ΔW have the same values as those of the symmetric ADF). First of all, it can drop a channel at λ_c when Λ_{13} and Λ_{23} are determined such that $\delta_{13} = 0$ and $\delta_{23} = 0$ at λ_c. Then, at λ_c, it can be shown that

$$a_1(y) = \frac{1}{2\kappa_a^2}\left[\kappa_{23}^2 + \kappa_{13}^2\cos\left(\sqrt{2}\kappa_a y\right)\right], \tag{20a}$$

$$a_2(y) = -\frac{\kappa_{13}^*\kappa_{23}}{\kappa_a^2}\sin^2\left(\frac{\kappa_a}{\sqrt{2}}y\right), \tag{20b}$$

where $\kappa_a^2 = (\kappa_{13}^2 + \kappa_{23}^2)/2$. T_{21} = 0 and T_{31} = 1 if $\kappa_{13} = \kappa_{23}$ and $y = \pi/(\sqrt{2}\kappa_a)$. When the width change of the left Si strip is 20 nm, $\kappa_{13} \approx \kappa_{23}$ if the width change of the right Si strip is

Optics EXPRESS

22.7 nm. The T_{21} and T_{31} spectra calculated by using Eqs. (16)–(18) are shown in Fig. 11(b). It can be confirmed that the asymmetric ADF works well.

Funding

National Research Foundation of Korea (NRF-2017R1A2B4007143).

References

1. A. F. J. Levi, "Silicon photonics' last-meter problem: Economics and physics still pose challenges to "fiber to the processor" tech," IEEE Spectr. **55**(9), 38–43 (2018).
2. Z. Zhou, R. Chen, X. Li, and T. Li, "Development trends in silicon photonics for data centers," Opt. Fiber Technol. **44**, 13–23 (2018).
3. W. Shi, X. Wang, W. Zhang, L. Chrostowski, and N. A. Jaeger, "Contradirectional couplers in silicon-on-insulator rib waveguides," Opt. Lett. **36**(20), 3999–4001 (2011).
4. H. Qiu, G. Jiang, T. Hu, H. Shao, P. Yu, J. Yang, and X. Jiang, "FSR-free add-drop filter based on silicon grating-assisted contradirectional couplers," Opt. Lett. **38**(1), 1–3 (2013).
5. W. Shi, X. Wang, C. Lin, H. Yun, Y. Liu, T. Baehr-Jones, M. Hochberg, N. A. F. Jaeger, and L. Chrostowski, "Silicon photonic grating-assisted, contra-directional couplers," Opt. Express **21**(3), 3633–3650 (2013).
6. W. Shi, H. Yun, C. Lin, M. Greenberg, X. Wang, Y. Wang, S. T. Fard, J. Flueckiger, N. A. F. Jaeger, and L. Chrostowski, "Ultra-compact, flat-top demultiplexer using anti-reflection contra-directional couplers for CWDM networks on silicon," Opt. Express **21**(6), 6733–6738 (2013).
7. W. Shi, H. Yun, C. Lin, J. Flueckiger, N. A. F. Jaeger, and L. Chrostowski, "Coupler-apodized Bragg-grating add-drop filter," Opt. Lett. **38**(16), 3068–3070 (2013).
8. H. Qiu, J. Jiang, P. Yu, D. Mu, J. Yang, X. Jiang, H. Yu, R. Cheng, and L. Chrostowski, "Narrow-band add-drop filter based on phase-modulated grating-assisted contra-directional couplers," J. Lightwave Technol. **36**(17), 3760–3764 (2018).
9. M. T. Boroojerdi, M. Ménard, and A. G. Kirk, "Bandwidth Tunable SOI Add-Drop Filter," in *Conference on Lasers and Electro-Optics, OSA Technical Digest (online)* (Optical Society of America, 2017), paper JTh2A.111.
10. S. K. Selvaraja, P. Jaenen, W. Bogaerts, D. Van Thourhout, P. Dumon, and R. Baets, "Fabrication of photonic wire and crystal circuits in silicon-on-insulator using 193-nm optical lithography," J. Lightwave Technol. **27**(18), 4076–4083 (2009).
11. H. Yamada, T. Chu, S. Ishida, and Y. Arakawa, "Optical add-drop multiplexers based on Si-wire waveguides," Appl. Phys. Lett. **86**(19), 191107 (2005).
12. J. Wang and L. R. Chen, "Low crosstalk Bragg grating/Mach-Zehnder interferometer optical add-drop multiplexer in silicon photonics," Opt. Express **23**(20), 26450–26459 (2015).
13. M. G. Saber, Z. Xing, D. Patel, E. El-Fiky, N. Abadía, Y. Wang, M. Jacques, M. Morsy-Osman, and D. V. Plant, "A CMOS compatible ultracompact silicon photonic optical add-drop multiplexer with misaligned sidewall Bragg gratings," IEEE Photonics J. **9**(3), 6601010 (2017).
14. J. Jiang, H. Qiu, G. Wang, Y. Li, T. Dai, D. Mu, H. Yu, J. Yang, and X. Jiang, "Silicon lateral-apodized add-drop filter for on-chip optical interconnection," Appl. Opt. **56**(30), 8425–8429 (2017).
15. Z. Wang, M. Ma, and L. R. Chen, "Integrated optical add-drop multiplexer in SOI based on mode selection and Bragg reflection," IEEE Photonics Technol. Lett. **30**(24), 2107–2110 (2018).
16. S. Paul, M. Kuittinen, M. Roussey, and S. Honkanen, "Multi-wavelength add-drop filter with phase-modulated shifted Bragg grating," Opt. Lett. **43**(13), 3144–3147 (2018).
17. M. Sodagar, R. Pourabolghasem, A. A. Eftekhar, and A. Adibi, "High-efficiency and wideband interlayer grating couplers in multilayer Si/SiO_2/SiN platform for 3D integration of optical functionalities," Opt. Express **22**(14), 16767–16777 (2014).
18. W. D. Sacher, Y. Huang, G.-Q. Lo, and J. K. S. Poon, "Multilayer silicon nitride-on-silicon integrated photonic platforms and devices," J. Lightwave Technol. **33**(4), 901–910 (2015).
19. J. C. C. Mak, Q. Wilmart, S. Olivier, S. Menezo, and J. K. S. Poon, "Silicon nitride-on-silicon bi-layer grating couplers designed by a global optimization method," Opt. Express **26**(10), 13656–13665 (2018).
20. G. Z. Masanovic, V. M. N. Passaro, and G. T. Reed, "Coupling to nanophotonic waveguides using a dual grating-assisted directional coupler," IEE Proc., Optoelectron. **152**(1), 41–48 (2005).
21. G. Masanovic, G. Reed, W. Headley, B. Timotijevic, V. Passaro, R. Atta, G. Ensell, and A. Evans, "A high efficiency input/output coupler for small silicon photonic devices," Opt. Express **13**(19), 7374–7379 (2005).
22. J. M. Chavez Boggio, D. Bodenmüller, T. Fremberg, R. Haynes, M. M. Roth, R. Eisermann, M. Lisker, L. Zimmermann, and M. Böhm, "Dispersion engineered silicon nitride waveguides by geometrical and refractive-index optimization," J. Opt. Soc. Am. B **31**(11), 2846–2857 (2014).
23. W. Huang and J. Hong, "A transfer matrix approach based on local normal modes for coupled waveguides with periodic perturbations," J. Lightwave Technol. **10**(10), 1367–1375 (1992).
24. S. K. Selvaraja, W. Bogaerts, P. Dumon, D. Van Thourhout, and R. Baets, "Subnanometer linewidth uniformity in silicon nanophotonic waveguide devices using CMOS fabrication technology," IEEE J. Sel. Top. Quantum Electron. **16**(1), 316–324 (2010).

Optics EXPRESS

25. L. Domash, M. Wu, N. Nemchuk, and E. Ma, "Tunable and switchable multiple-cavity thin film filters," J. Lightwave Technol. **22**(1), 126–135 (2004).
26. M. A. Popovic, T. Barwicz, M. S. Dahlem, F. Gan, C. W. Holzwarth, P. T. Rakich, M. R. Watts, H. I. Smith, F. X. Kärtner, and E. P. Ippen, "Hitless-reconfigurable and bandwidth-scalable silicon photonic circuits for telecom and interconnect applications," in *Optical Fiber Communication Conference/National Fiber Optic Engineers Conference, OSA Technical Digest (CD)* (Optical Society of America, 2008), paper OTuF4.
27. D. Aguiar, M. Milanizadeh, E. Guglielmi, F. Zanetto, M. Sampietro, F. Morichetti, and A. Melloni, "Automatic tuning of hitless add-drop filter array based on microrings," in *Advanced Photonics 2018, OSA Technical Digest (online)* (Optical Society of America, 2018), paper IW4I.8.
28. C. Ríos, M. Stegmaier, P. Hosseini, D. Wang, T. Scherer, C. D. Wright, H. Bhaskaran, and W. H. P. Pernice, "Integrated all-photonic non-volatile multi-level memory," Nat. Photonics **9**(11), 725–732 (2015).
29. M. Wuttig, H. Bhaskaran, and T. Taubner, "Phase-change materials for non-volatile photonic applications," Nat. Photonics **11**(8), 465–476 (2017).
30. K. J. Miller, R. F. Haglund, and S. M. Weiss, "Optical phase change materials in integrated silicon photonic devices: review," Opt. Mater. Express **8**(8), 2415–2429 (2018).
31. Q. Zhang, Y. Zhang, J. Li, R. Soref, T. Gu, and J. Hu, "Broadband nonvolatile photonic switching based on optical phase change materials: beyond the classical figure-of-merit," Opt. Lett. **43**(1), 94–97 (2018).
32. Y. Kim and M.-S. Kwon, "Mid-infrared subwavelength modulator based on grating-assisted coupling of a hybrid plasmonic waveguide mode to a graphene plasmon," Nanoscale **9**(44), 17429–17438 (2017).